

**Supplemental Material for  
Transient creep on the Xidatan (Tibet) fault driven by viscoelastic relaxation  
following the 2001 Kokoxili earthquake**

**Dezheng Zhao<sup>1</sup>, Chunyan Qu<sup>\*1</sup>, Xinjian Shan<sup>1</sup>, Roland Bürgmann<sup>2</sup>, Han  
Chen<sup>1</sup>, Kathryn Materna<sup>2†</sup>**

<sup>1</sup>State Key Laboratory of Earthquake Dynamics, Institute of Geology, China  
Earthquake Administration, Beijing, 100029, China

<sup>2</sup>Department of Earth and Planetary Science and Berkeley Seismology Lab,  
University of California, Berkeley, CA94708, USA

<sup>†</sup>Now at: U.S. Geological Survey, Earthquake Science Center, Moffett Field, CA  
94035, USA

\* Contact author: Chunyan Qu ([dqchy@ies.ac.cn](mailto:dqchy@ies.ac.cn))

**This supplement file includes:**

**Texts S1 to S4**

**Figures S1 to S11**

## Text S1. InSAR data analysis using two basis functions

We use two basis functions (Barbot et al., 2009; Tang et al., 2019; 2020) to quantitatively evaluate the potentially respective contributions from transient frictional afterslip and viscoelastic relaxation driven by the coseismic stress perturbations induced by the 2001 Mw7.8 Kokoxili earthquake. The two basis functions are used to isolate deformation associated with the localized afterslip and distributed viscoelastic relaxation deformation based on their respective constitutive laws (Tang et al., 2019; 2020).

The postseismic deformation following this earthquake, involving various spatiotemporal scales, processes and mechanisms, has been extensively investigated, and it is widely accepted that viscoelastic relaxation in the lower crust is the dominant postseismic process (e.g., Liu et al., 2019; Ryder et al., 2011; Wen et al., 2012; Zhao et al., 2021). For large strike-slip earthquakes, the pattern, wavelength and magnitude of surface deformation produced by deep frictional afterslip and viscoelastic relaxation are typically similar (e.g., Freed et al., 2006). Therefore, the unique separation of the respective displacements of (deep) afterslip and viscoelastic relaxation remains one of the most pressing challenges in postseismic deformation studies. Consideration of postseismic vertical displacements and using horizontal displacements in the (very) far-field, featuring distinguishable wavelengths of surface deformation produced by afterslip in the downdip shear zone versus viscous flow in the lower crust/upper mantle, helps to better separate the components of deformation generated by afterslip and viscoelastic relaxation (e.g., Diao et al., 2018; Pollitz, 2015).

For the InSAR time series following the 2001 Kokoxili earthquake, we rely on analytical equations incorporating two basis functions to identify and separate the mixed two deformation components. First, we only analyze the InSAR time series observed by Envisat/ASAR data covering the Xidatan fault (T90 on descending track). These observations span a time period of 2003-2010, during which deep afterslip has been suggested to be less important and viscoelastic relaxation deformation is dominant (e.g., Ryder et al., 2011; Zhao et al., 2021). Second, deep stress-driven afterslip that occurred on the downdip extension of the Kusai Hu fault likely produced minor surface deformation in proximity to the Xidatan fault, compared with viscoelastic relaxation prevalent in the far deeper lower crust and upper mantle (Zhao et al., 2021).

We describe the two-basis-function approach in detail as follows. The method assumes that time-dependent postseismic displacement can be mathematically described as a linear combination of two temporal basis functions explaining the short- and long-term post-earthquake processes at a decadal scale, consistent with afterslip and viscous flow, respectively. The two basis functions ( $B_1$ ,  $B_2$ ) accounting for the transient and steady-state processes are described as

$$B_1(t) = 1 - \frac{2}{k} \coth^{-1} \left[ \exp \left( \frac{t}{t_{c1}} \right) \coth \left( \frac{2}{k} \right) \right], k > 0 \quad (1)$$

$$B_2(t) = 1 - \exp \left( \frac{-t}{t_{c2}} \right) \quad (2)$$

where  $t_{c1}$  and  $t_{c2}$  represent the characteristic time determining the time scale of the postseismic displacement evolution;  $k$  is a constant, also called the degree of nonlinearity, used to control the velocity of the transient afterslip in a rate-and-state friction framework (Barbot et al., 2009);  $t$  is the time after the earthquake. The best-fitting parameters ( $t_{c1}$ ,  $t_{c2}$ ,  $k$ ) in the two basis functions are obtained by jointly searching for the minima of root-mean-square (RMS) between model predictions and InSAR timeseries observations on descending track 90 (Figures S3, S4).

We find that only the long-term deformation with  $t_{c2} = 15$  years is well constrained, indicating that our InSAR observations (T90) primarily captured time-dependent viscoelastic relaxation deformation during 2003-2010. The result is consistent with the earlier modeling work by Zhao et al. (2021), suggesting that afterslip within the upper crust (<20 km, mostly on the sub-parallel Kunlun Pass fault to the south) decayed more rapidly (shorter duration) than the viscoelastic relaxation in the lower crust/upper mantle (>20 km), and thus the postseismic deformation of afterslip do not significantly affect the area around the Xidatan fault during 2003-2010. The analysis of two basis functions supports the view that the diagnostic and localized displacement gradient across the Xidatan fault during 2003-2010 due to shallow creep is not due to afterslip following the Kokoxili earthquake. Considering that viscoelastic relaxation is the dominant postseismic deformation process, the observed gradient is likely driven by the more enduring lower crustal viscoelastic relaxation process.

## Test S2 InSAR data analysis using T-mode PCA transformation

We apply T-mode PCA (Principal Component Analysis, Chaussard et al., 2014) in order to isolate the dominant spatiotemporal evolution patterns of the postseismic InSAR displacement timeseries. The T-mode PCA transformation is helpful to retrieve and characterize distinct deformation sources, including the tectonic deformation (i.e., postseismic and interseismic deformation) and residual atmospheric error sources. Moreover, the method enables us to reduce the effective number of separate components or sources in the InSAR timeseries without missing the characteristics and it has been quite widely adopted in the analysis of timeseries observations for GPS and InSAR data (e.g., Gualandi et al. 2020; Marshall et al., 2013; Shi et al., 2021).

The data matrix from the InSAR timeseries is organized in a matrix  $X$  with a dimension of  $(m \times n)$ , which corresponds to the number of pixels ( $m$ ) observed at  $n$  time steps. We rely on the SVD transformation to achieve the PCA analysis, as described below.

$$\begin{cases} P = XW \\ X = U\Sigma W^T \end{cases}$$

Useful outputs from the above transformation include the PC scores ( $P, m \times n$ ), the eigenvectors ( $W, n \times n$ ) and the eigenvalues embedded in the diagonal matrix ( $\Sigma, m \times n$ ). The PC score matrix from  $P$  and the eigenvectors from  $W$  correspond to the spatial patterns and temporal evolutions of deformation, respectively. We retain the first three PCs and discard the subsequent PCs. The results indicate that PC1-PC3 explain >95.5% (PC1>68%) of the data variance, which is sufficient to represent the underlying data characteristics and structure.

### **Text S3. Coulomb stress change calculation**

The coseismic slip distribution of the 2021 Mw 7.8 Kokoxili earthquake is from Zhao et al. (2021). The inverted coseismic slip distribution is constrained by coseismic InSAR and GPS observations. In the coseismic slip model, the ruptured faults include the Kusai Hu fault and the Kunlun Pass fault.

The combined postseismic model, invoking afterslip and viscoelastic relaxation, is constrained by GPS (2001-2002) and InSAR (2003-2010) measurements. Afterslip is driven by coseismic stress changes and modeled in a rate- and state-dependent friction framework (Barbot and Fialko, 2010; Barbot et al., 2009). For the viscoelastic relaxation, the applied model has dimensions of 900 km  $\times$  800 km across and along the strike of the Kunlun fault, respectively. The base depth of the upper mantle is set to 200 km. The model domain is divided into a series of 30  $\times$  30  $\times$  10 km cuboids. The Moho depth beneath the Tibetan Plateau to the south and the Qaidam Basin to the north is fixed at 70 and 60 km, respectively. We apply a bi-viscous Burgers rheology body with a Kelvin solid in series with a Maxwell fluid, with a transient viscosity ( $\eta_1$ ) of the Kelvin element and a steady-state viscosity ( $\eta_2$ ) of the Maxwell element for the lower crust and upper mantle. The shear modulus is set to 40 GPa and Poisson's ratio is 0.25. The best-fitting transient and steady-state viscosities in the Tibetan lower crust in the combined model are  $5 \times 10^{18}$  Pas and  $4 \times 10^{19}$  Pas, respectively, which are corresponding to transient and steady-state relaxation times of 4 and 31.7 years, respectively (Zhao et al., 2021). Both the transient and steady state viscoelastic relaxation times are greater than that of the afterslip on the Kunlun Pass fault with an inferred logarithmic decay time of 1.6 years. Accordingly, the dominant postseismic processes in the aftermath of the Kokoxili include deep afterslip (>20 km depth) on the Kusai Hu fault, afterslip (<20 km) on the Kunlun Pass fault, and more enduring viscoelastic relaxation in the lower crust and upper mantle. See more details related to the combined postseismic model in Zhao et al. (2021).

In our postseismic deformation model, we do not include the Xidatan fault to resolve for the triggered aseismic slip on the fault due to the following considerations. First, determining the

creep distribution on the Xidatan fault requires knowledge of areas with velocity strengthening behavior and frictional parameters in the stress-driven creep model. However, the fault frictional behavior and properties of the Xidatan fault have not been well investigated. Second, incorporating the stress-driven creep on the Xidatan fault in the three-dimensional postseismic deformation model will increase the number of free parameters of the model, but the current limited postseismic observations, especially during 2001-2002, cannot robustly address the complicated trade-off relationships between various parameters.

We compute the Coulomb stress change resolved onto the receiver fault, the Xidatan fault, having the same geometry with a dip of  $90^\circ$ , a rake angle of  $0^\circ$  (left-lateral strike-slip motion) and rectangular sub-fault patches. We calculate the time-dependent strain and stresses driven by coseismic slip, afterslip and viscoelastic relaxation. We calculate the Coulomb stress changes on the receiver fault plane. We use a suite of numerical three-dimensional models to investigate how coseismic slip on the Kusai Hu fault, coseismic slip on both the Kuasai Hu and the Kunlun Pass faults, and afterslip and viscoelastic relaxation change the stress state and drive the shallow creep on the Xidatan fault.

#### **Text S4. InSAR reference frame transformation and 3-D displacement reconstruction**

Our Sentinel-1 InSAR observations during 2015-2020 on descending and ascending tracks around the Xidatan fault demonstrate a smooth velocity gradient across the fault, reflecting deformation on a strongly coupled Xidatan fault. We apply a transformation of the InSAR line-of-sight (LOS) velocities on the ascending and descending tracks into a Eurasia-fixed reference frame, following the method outlined in Hussain et al. (2016), utilizing the horizontal components of the published interseismic GPS velocities from Wang and Shen (2020).

We determine the best fit second-order polynomial through the residual velocities between InSAR velocities and interpolated LOS-converted GPS velocities. We then remove this from the InSAR velocities to transform the LOS velocities into the Eurasia-fixed reference frame. The resultant InSAR velocity field is tied to the spatially sparse GPS observations, but this transformation preserves small-scale ( $\leq 100$  km) features in the InSAR deformation field (e.g., Weiss et al., 2020).

To obtain the horizontal components (east-west and north-south) of surface motion from the ascending and descending InSAR LOS measurements, we adopt the approach outlined in Hussain et al. (2016) and Weiss et al. (2020) to decompose LOS velocities into east-west and north-south displacements for every grid element where both ascending and descending observations are available. Since the InSAR line-of-sight observations are not sensitive to the north-south component of surface deformation, the interpolated north-south velocity field from interseismic GPS velocities (Wang and Shen, 2020) is used as an *a priori* constraint during the

calculation of the other two displacement components (east-west and vertical displacements). We use both north-south and east-west components of the horizontal velocity field to derive the fault-parallel velocities. Due to the nearly east-west trend of the Xidatan fault, the dominant contribution to the resultant fault-parallel velocities is from east-west displacements generated by the left-lateral strike-slip motion of the fault.

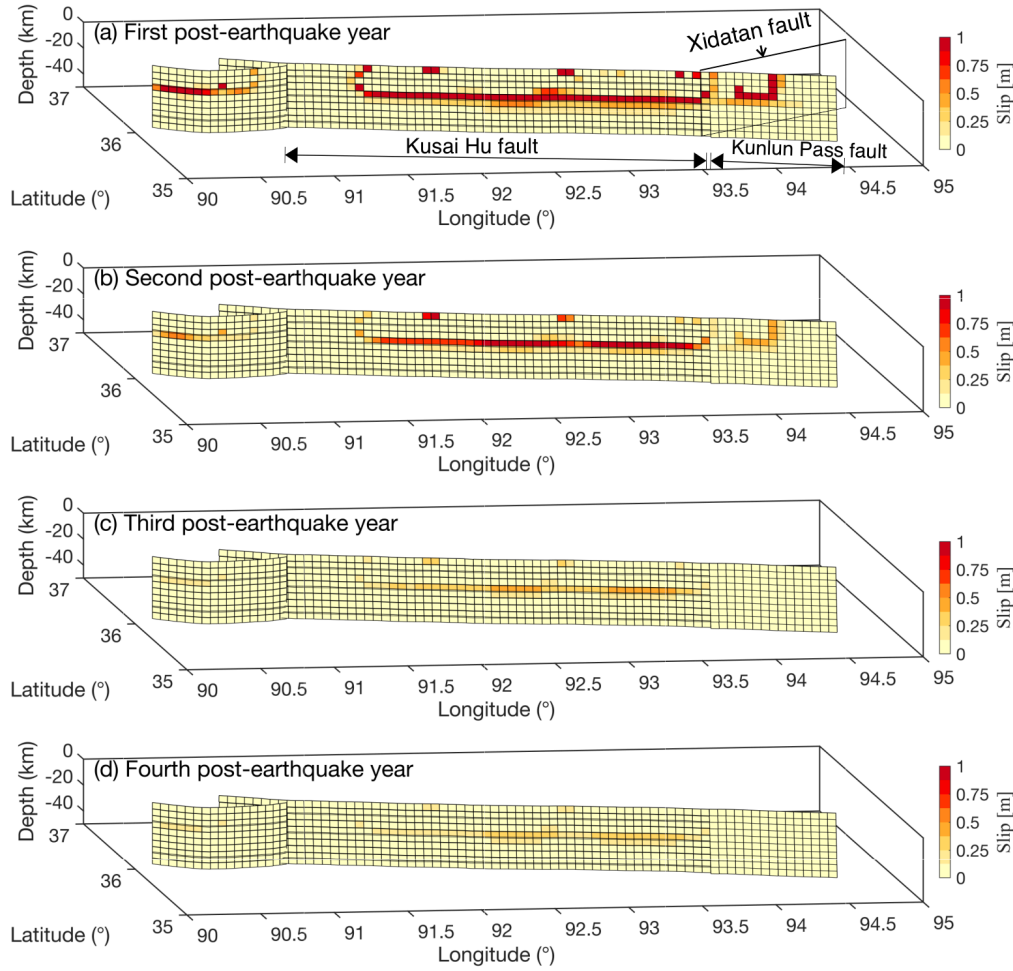


**Figure S1.** Snapshots of stress-driven afterslip distributions on the Kusai Hu fault (afterslip distributed at depth >20 km) and the Kunlun Pass fault (afterslip distributed at depth <20 km) in the sequential postseismic periods following the 2001 Kokoxili earthquake, using the combined postseismic deformation model in Zhao et al. (2021). The black rectangle in (a) schematically indicates the location of the Xidatan fault. The results highlight the relatively long-lived deep afterslip on the Kusai Hu fault.

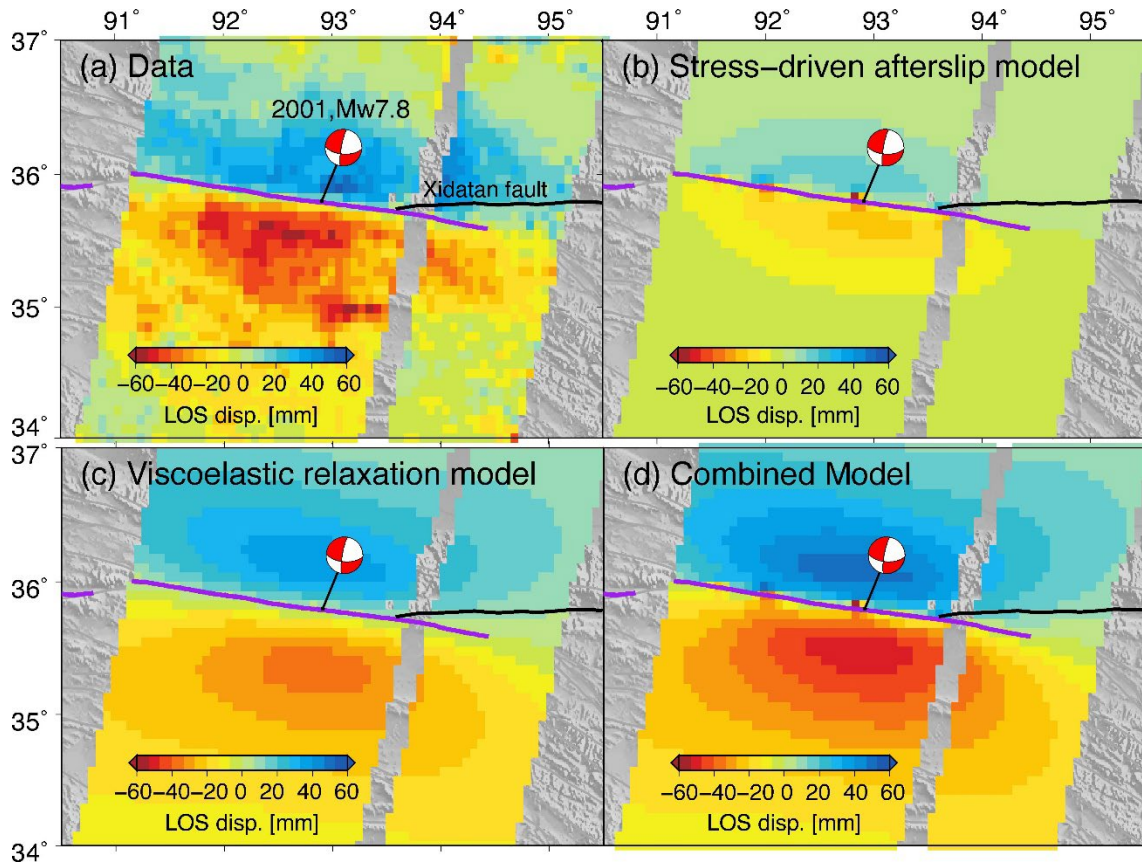


**Figure S2.** InSAR observations (a, spanning 20030714-20100920) and deformation contributions in the same time window from deep afterslip ( $>20$  km, mostly on the deep extension of the Kusai Hu fault) and viscoelastic relaxation of the lower crust and upper mantle (b-d) after the 2001 Mw7.8 Kokoxili earthquake. The results indicate that afterslip on the Kusai Hu fault and the Kunlun Pass fault driven by the coseismic stress perturbations are not likely responsible for the observed sharp displacement gradient during the 2003-2010 InSAR observation period across the Xidatan fault. Purple lines illustrate the surface rupture trace of the 2001 Kokoxili earthquake. Black line denotes the surface trace of the Xidatan fault.

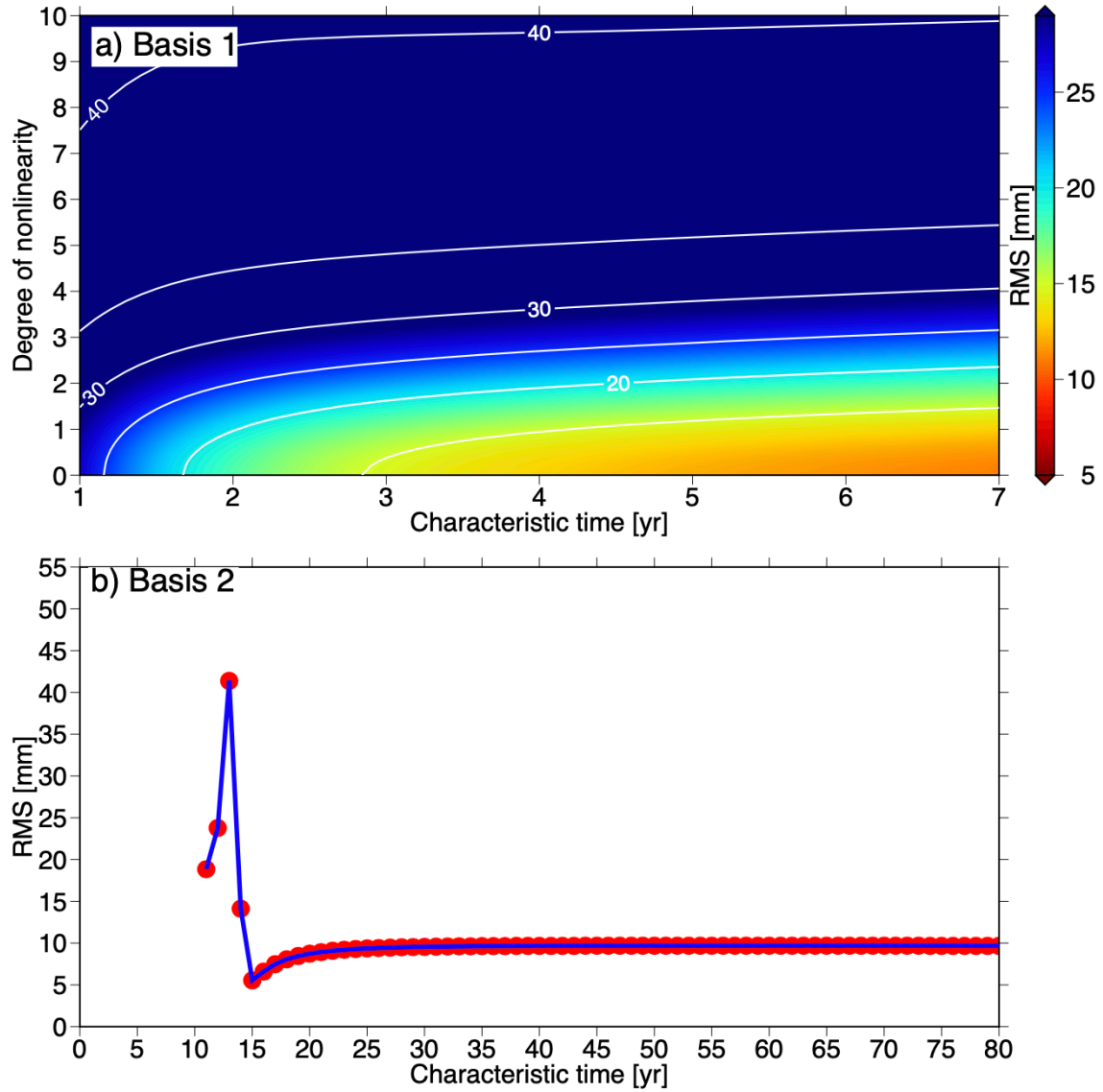


**Figure S3.** Root-mean-square misfits between model predictions and InSAR timeseries observations (T90, also shown in Figure S2a) using the basis function 1 (a) and function 2 (b). We search for three best-fitting parameters, including the characteristic times ( $t_{c1}$ ,  $t_{c2}$ ) and the degree of nonlinearity ( $k$ ). Only the characteristic time in function 2 is robustly constrained. The preferred parameterization of  $t_{c2} = 15$  years with  $\text{RMS} = 5$  mm is utilized.



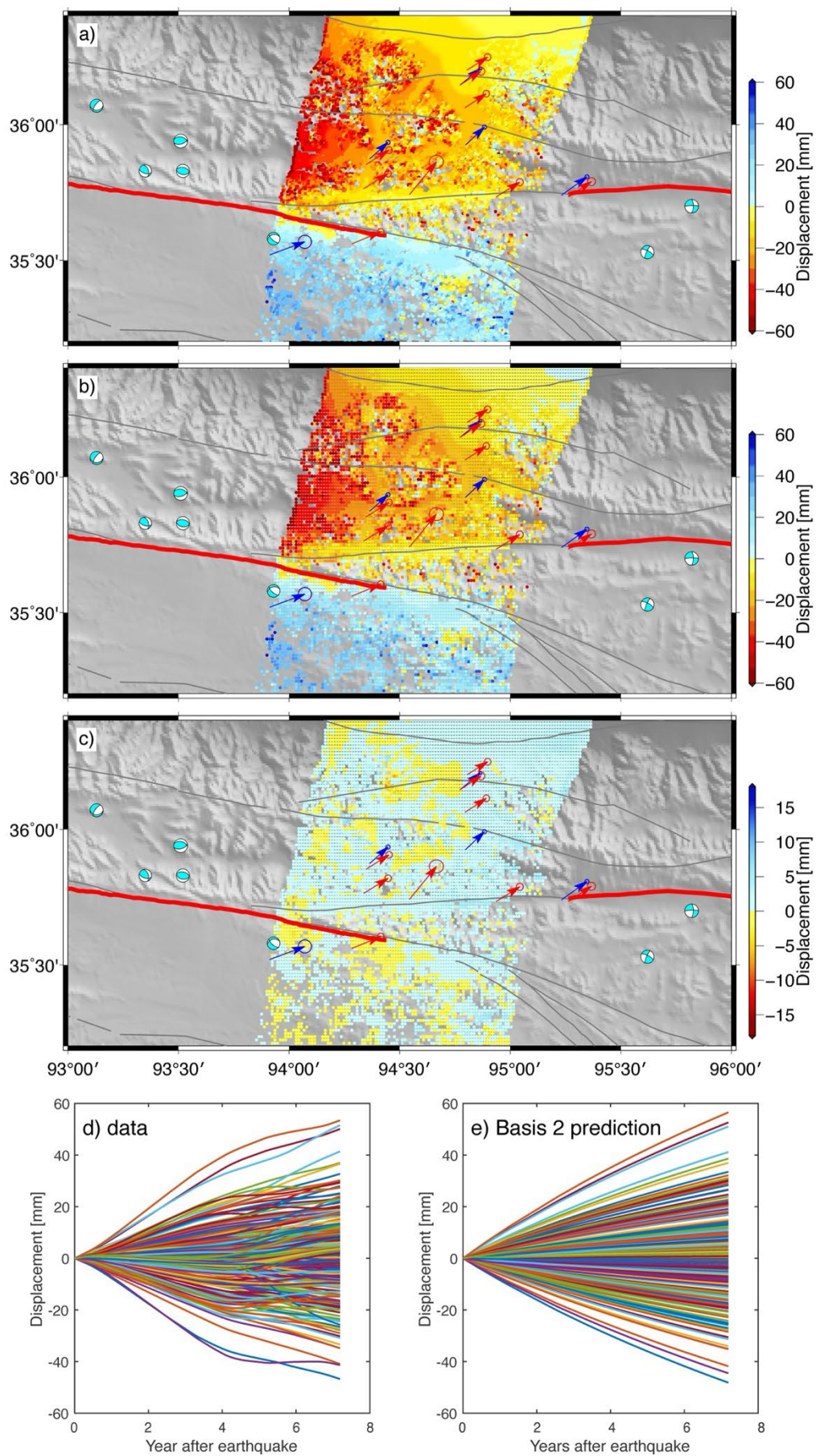


**Figure S4.** Observations of cumulative InSAR displacement from 20030714 to 20100920 (a) and displacement components (b, basis function 2; c, basis function 1), decomposed using the two basis functions. Thin grey lines indicate active faults; red lines denote spatial extents of two historical ruptures during the 2001 Mw7.8 Kokoxili earthquake and 1963 Mw7.1 earthquake. Red (Liu et al., 2019) and blue (Wang and Shen, 2020) arrows are interseismic secular velocities in a fixed Eurasia reference frame. (d, e) Data and model predictions using the best fitting parameters of basis function 2 (Figure S3b) for the InSAR observations during 2003-2010. In d) and e), each line represents the time series of each pixel in the deformation field.

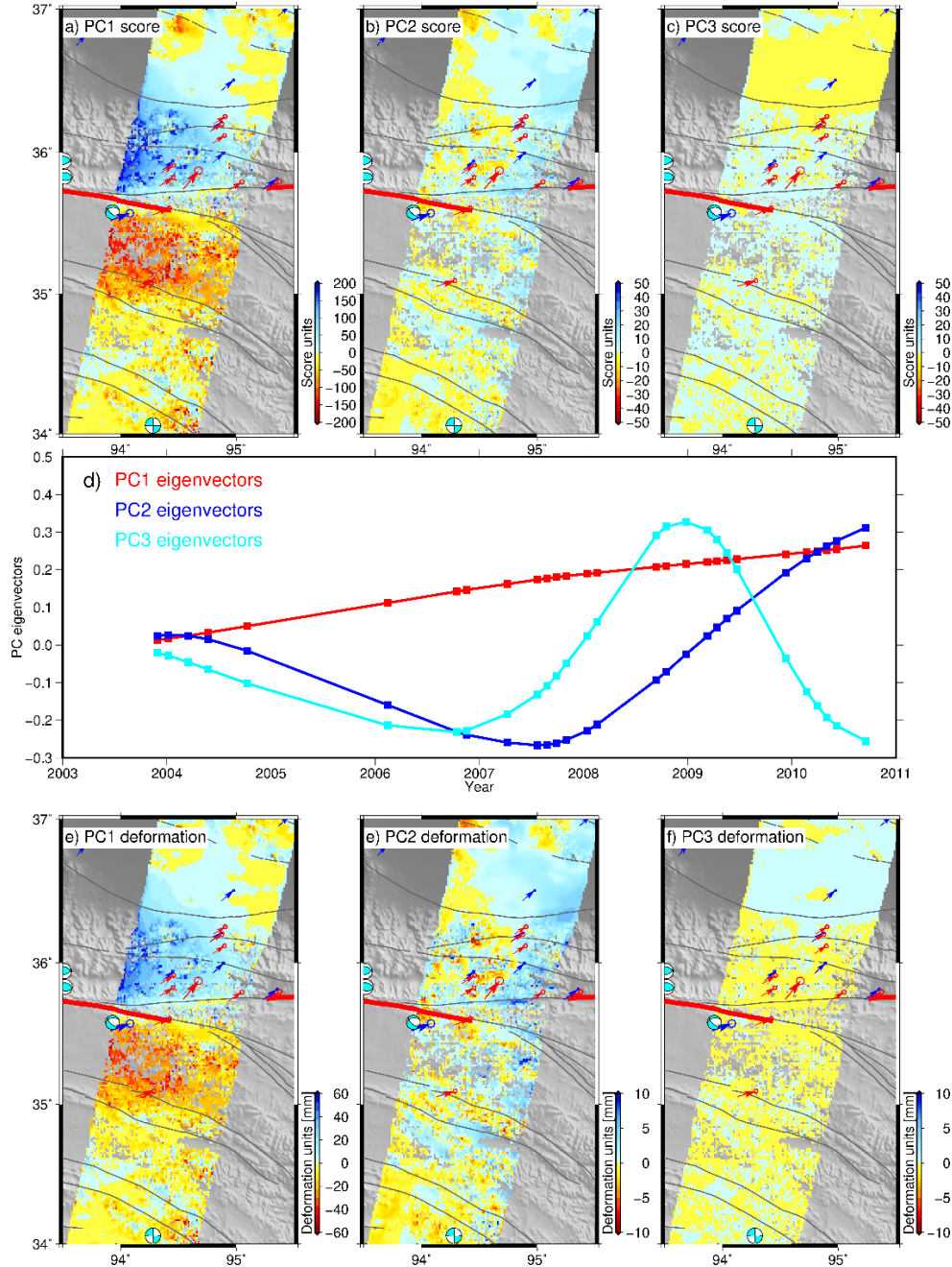




**Figure S5.** T-mode PCA transformation results in descending ASAR track 90. (a-c) PC1, PC2 and PC3 score maps illustrating the spatial deformation pattern spanning 2003-2010 around the Xidatan fault. (d) Eigenvectors of PC1, PC2, and PC3 demonstrating the temporal evolution patterns of postseismic deformation. (e-f) Isolated deformation maps at the last acquisition of SAR images converted from score maps and eigenvectors.

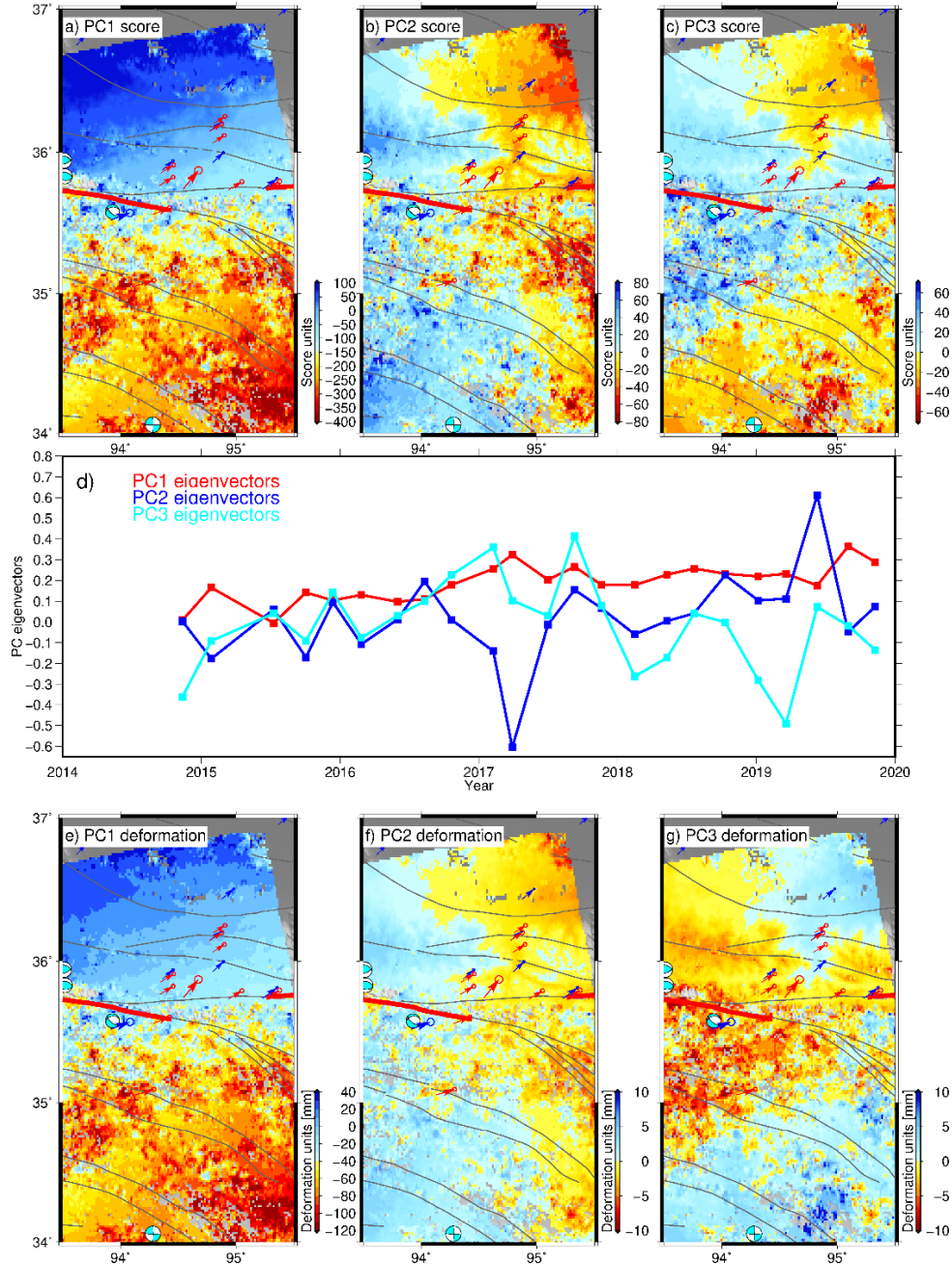


**Figure S6.** T-mode PCA transformation results on ascending Sentinel-1 track 70. (a-c) PC1, PC2 and PC3 score maps illustrating the spatial deformation pattern spanning 2015-2020 around the Xidatan fault. (d) Eigenvectors of PC1, PC2, PC3 demonstrating the temporal evolution patterns of postseismic deformation. (e-f) Isolated deformation maps converted from score maps and eigenvectors at the last acquisition of SAR images.

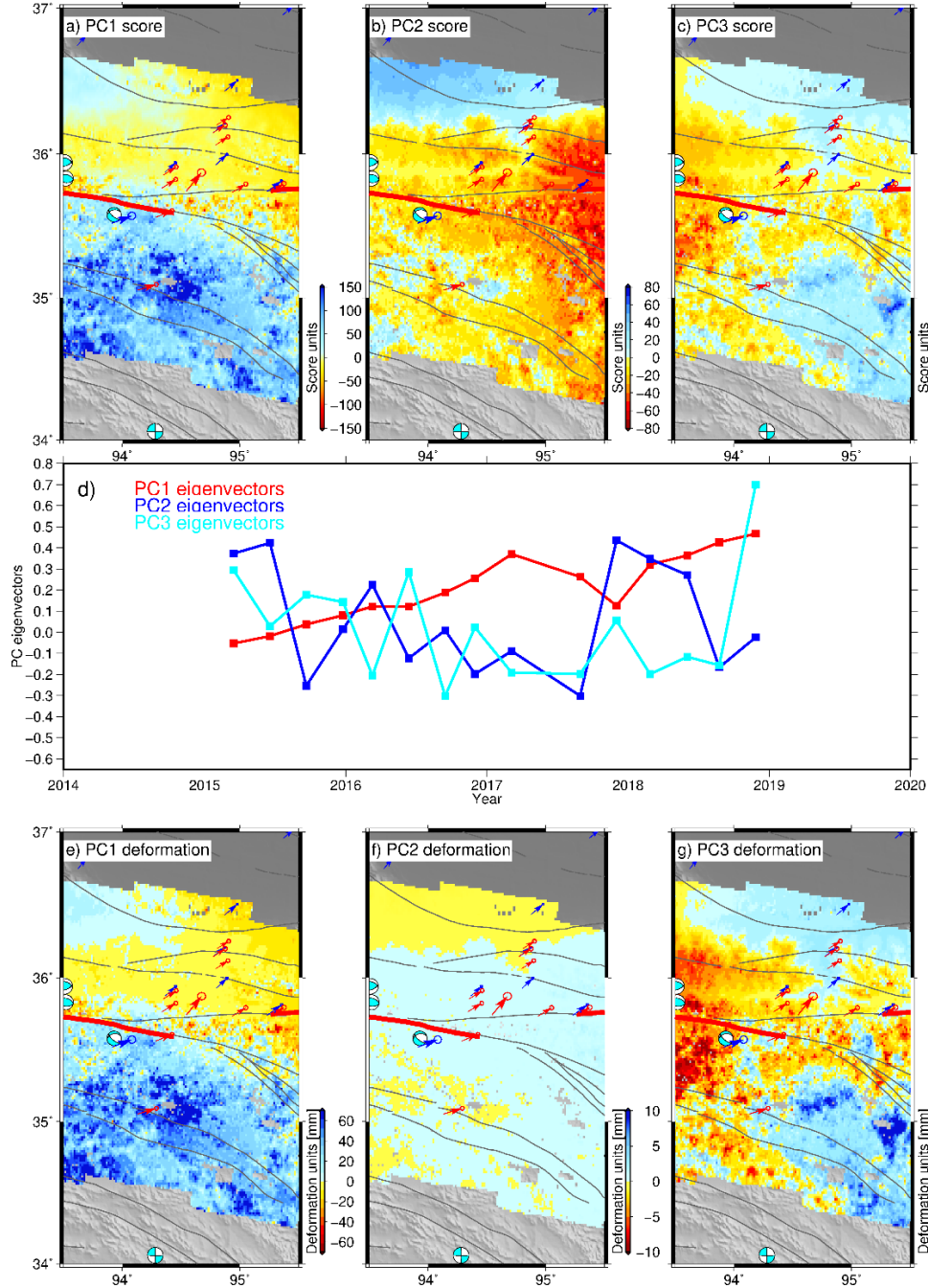


**Figure S7.** T-mode PCA transformation results on descending Sentinel-1 track 77. (a-c) PC1, PC2 and PC3 score maps illustrating the spatial deformation pattern spanning 2015-2020 around the Xidatan fault. (d) Eigenvectors of PC1, PC2 and PC3 demonstrating the temporal evolution patterns of postseismic deformation. (e-f) Isolated deformation maps converted from score maps and eigenvectors at the last acquisition of SAR images.

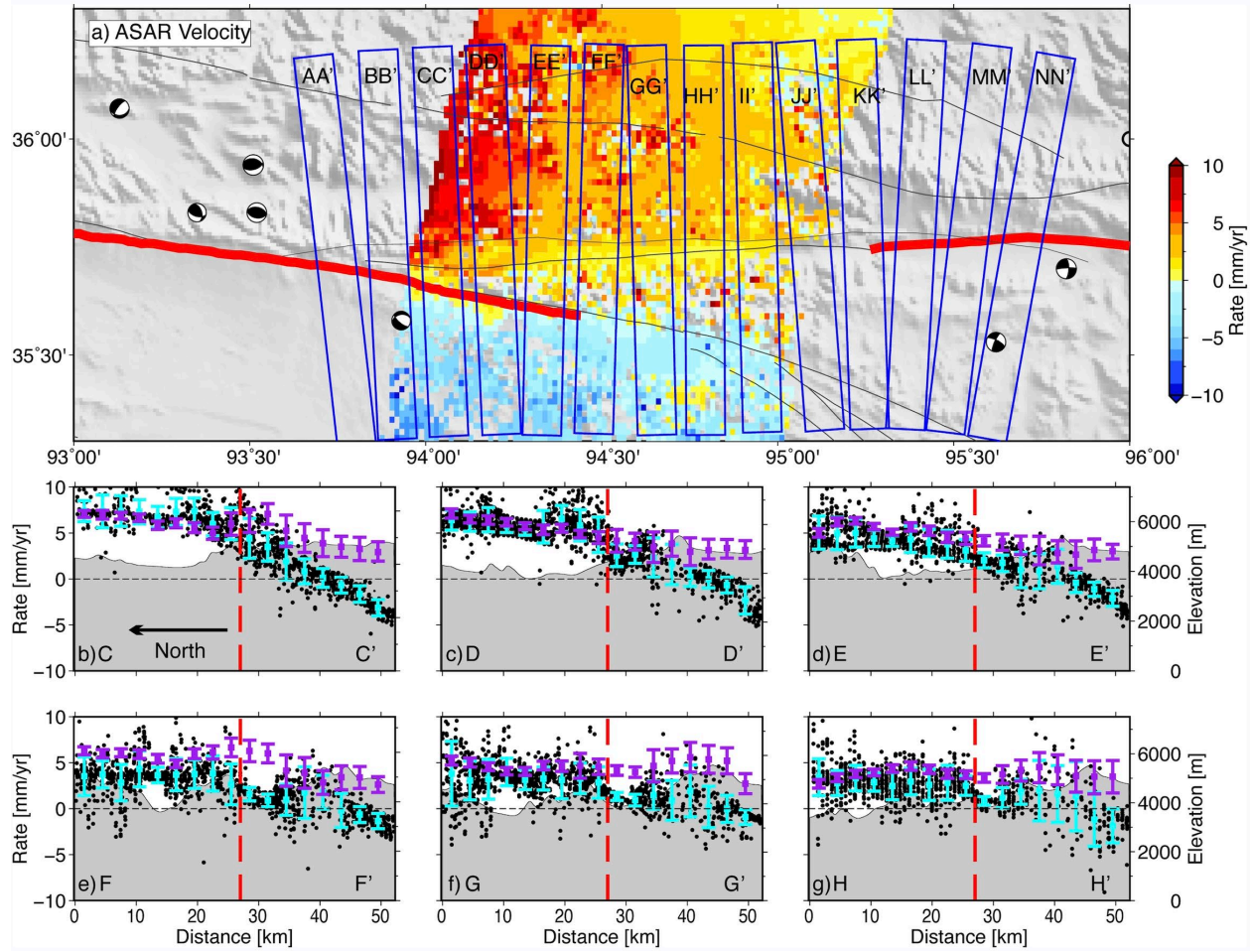


**Figure S8.** A comparison of InSAR observations of descending Envisat (2003-2010, T90) and descending Sentinel-1 data (2015-2020, T77). Blue boxes show the sliding window used to derive velocity profiles. (b-g) Postseismic LOS velocity profiles across the Xidatan fault. Black points show InSAR displacements from 2003-2010 descending-orbit Envisat data. Binned averages are shown every 2.5 km along the profile as cyan (Envisat data) and purple (Sentinel-1 data) squares with 2-sigma error bars.

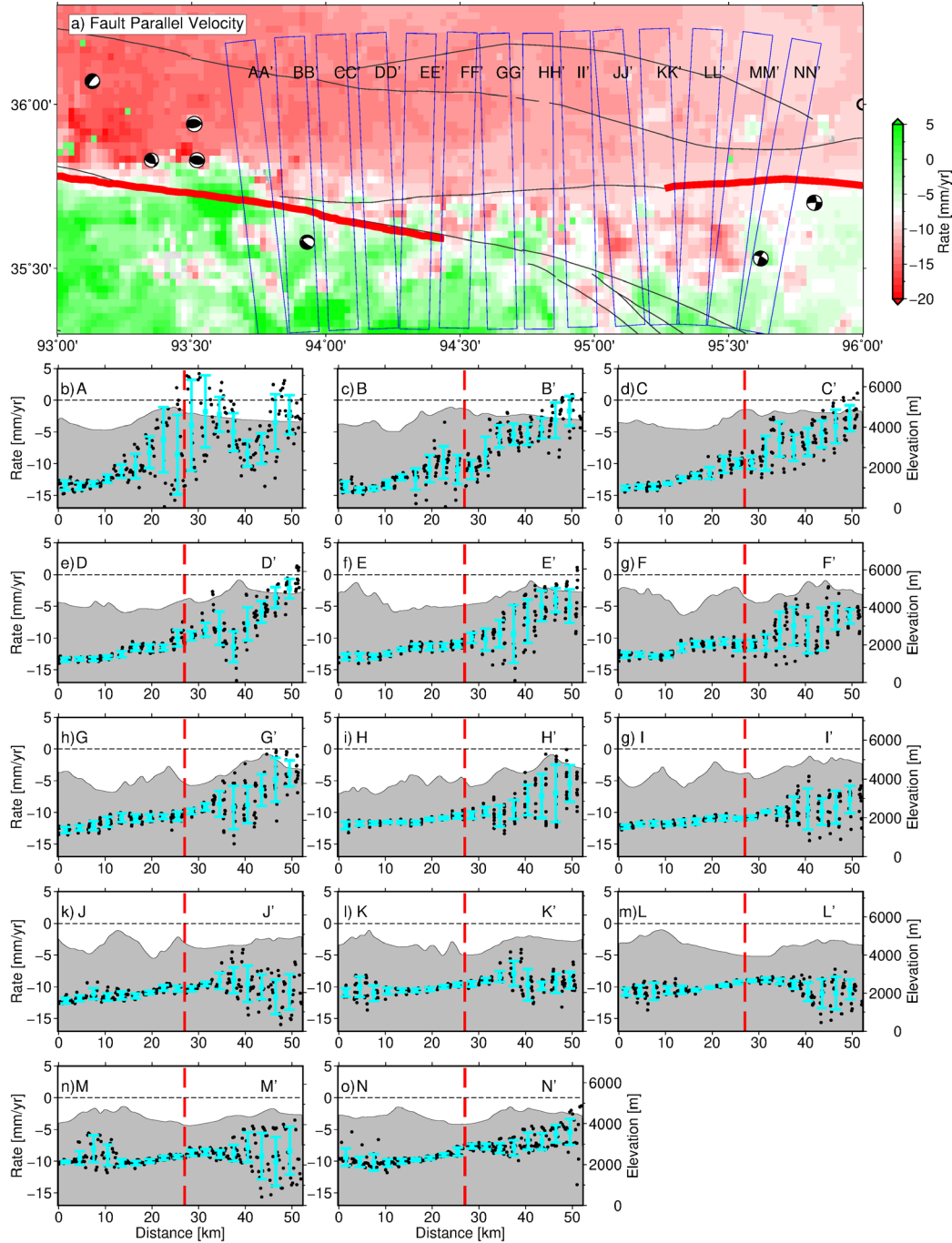


**Figure S9.** Fault-parallel velocity from 2015-2020 Sentinel-1 data and fourteen velocity profiles along the Xidatan fault. The blue boxes used to derive displacement profiles are the same as in 2b-2o. Black points show InSAR velocities. The binned averages every 2.5 km along the profile (cyan squares) with 2-sigma error bars within each bin. Red dashed lines denote the location of the Xidatan fault.



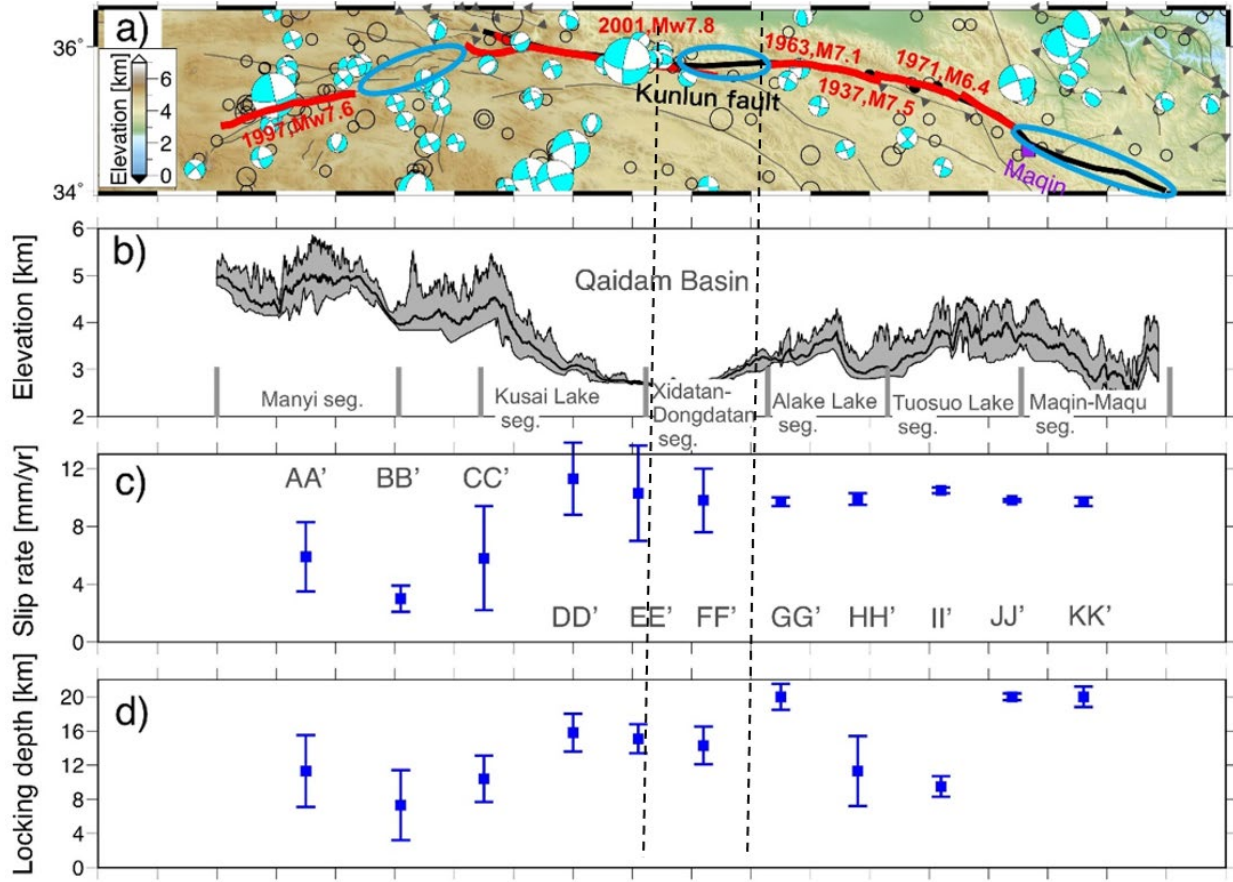


**Figure S10.** Fault geometry, historical ruptures (red bold lines, a) and variations in elevation (b), fault slip rate (c) and locking depth (d) along the Kunlun fault from Zhao et al. (2022). (AA' – KK') are eleven locations along the fault. Fault slip rate and locking depth are derived from Sentinel-1 fault-parallel velocities during 2015-2020, corrected for postseismic deformation from the Kokoxili earthquake, using a two-dimensional elastic screw dislocation model (Savage and Burford, 1973). For the fault slip rate and locking depth estimates of the Xidatan fault, we consider the kinematic model incorporating the deformation contribution from both the Xidatan fault and the subparallel Kunlun Pass fault. Light blue ellipses in (a) indicate three historical seismic gaps of the Kunlun fault, including the Xidatan fault. The results highlight the interseismic locking on the Xidatan fault and can be compared to the 3-D kinematic coupling distribution in Figure S11.

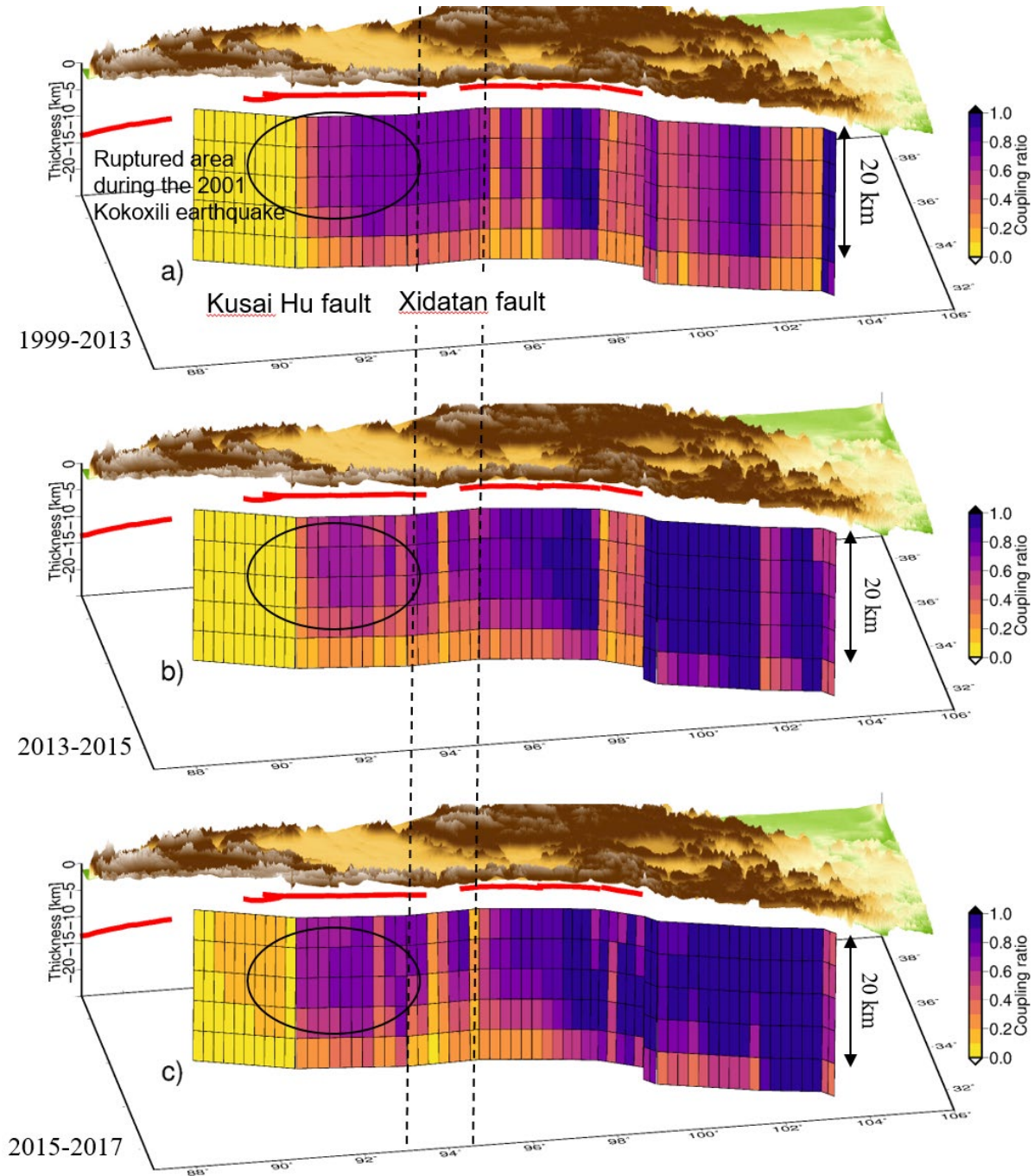


**Figure S11.** Interseismic coupling spanning 1999-2013, 2013-2015, and 2015-2017, distributed along the whole Kunlun fault, from Zhu et al. (2021). Red lines illustrate historically ruptured segments. The geodetic imaging of kinematic coupling of the Kunlun fault is determined by secular GPS velocities during 1999-2013 and leveling measurements spanning 1970-2013. The detailed methodology can be found in Zhu et al. (2021). Note that the GPS dataset during 1999-2013 utilized to constrain the model have considered and removed the deformation contributions from coseismic and postseismic displacements generated by the 2001 Kokoxili earthquake. The coupling distribution in (a) thus offers a nominal interseismic coupling distribution on the



Xidatan fault. Although some minor residual postseismic deformation still exists (see data comparisons in Zhao et al., 2022), the estimates of fault coupling ratio likely provide a lower bound in Zhu et al. (2021). Some narrow stripes of low coupling from top to bottom around the Xidatan fault in (a-c) are not kinematically reliable due to the sparse GPS data constraints on the surface.

## References Cited:

- Barbot, S., & Fialko, Y. (2010). A unified continuum representation of post-seismic relaxation mechanisms: semi-analytic models of afterslip, poroelastic rebound and viscoelastic flow. *Geophysical Journal International*, 182(3), 1124-1140.
- Barbot, S., Fialko, Y., & Bock, Y. (2009). Postseismic deformation due to the Mw 6.0 2004 Parkfield earthquake: Stress - driven creep on a fault with spatially variable rate-and-state friction parameters. *Journal of Geophysical Research: Solid Earth*, 114(B7).
- Chaussard, E., Burgmann, R., Shirzaei, M., Fielding, E. J., & Baker, B. (2014). Predictability of hydraulic head changes and characterization of aquifer-system and fault properties from InSAR-derived ground deformation. *Journal of Geophysical Research: Solid Earth*, 119(8), 6572-6590.
- Diao, F., Wang, R., Wang, Y., Xiong, X., & Walter, T. R. (2018). Fault behavior and lower crustal rheology inferred from the first seven years of postseismic GPS data after the 2008 Wenchuan earthquake. *Earth and Planetary Science Letters*, 495, 202-212.
- Freed, A. M., Bürgmann, R., Calais, E., Freymueller, J., & Hreinsdóttir, S. (2006). Implications of deformation following the 2002 Denali, Alaska, earthquake for postseismic relaxation processes and lithospheric rheology. *Journal of Geophysical Research: Solid Earth*, 111(B1).
- Gualandi, A., Liu, Z., & Rollins, C. (2020). Post-large earthquake seismic activities mediated by aseismic deformation processes. *Earth and Planetary Science Letters*, 530, 115870.
- Hussain, E., Hooper, A., Wright, T. J., Walters, R. J., & Bekaert, D. P. (2016). Interseismic strain accumulation across the central North Anatolian Fault from iteratively unwrapped InSAR measurements. *Journal of Geophysical Research: Solid Earth*, 121(12), 9000-9019.
- Liu, S., Xu, X., Klinger, Y., Nocquet, J. M., Chen, G., Yu, G., & Jónsson, S. (2019). Lower crustal heterogeneity beneath the northern Tibetan Plateau constrained by GPS measurements following the 2001 Mw7. 8 Kokoxili earthquake. *Journal of Geophysical Research: Solid Earth*, 124(11), 11992-12022.
- Marshall, S. T., Funning, G. J., & Owen, S. E. (2013). Fault slip rates and interseismic deformation in the western Transverse Ranges, California. *Journal of Geophysical Research: Solid Earth*, 118(8), 4511-4534.

- Pollitz, F. F. (2015). Postearthquake relaxation evidence for laterally variable viscoelastic structure and water content in the Southern California mantle. *Journal of Geophysical Research: Solid Earth*, 120(4), 2672-2696.
- Ryder, I., Bürgmann, R., & Pollitz, F. (2011). Lower crustal relaxation beneath the Tibetan Plateau and Qaidam Basin following the 2001 Kokoxili earthquake. *Geophysical Journal International*, 187(2), 613-630.
- Savage, J. C., Burford, R. O. (1973). Geodetic determination of relative plate motion in central California. *Journal of Geophysical Research*, 78(5), 832-845.
- Shi, G., Ma, P., Hu, X., Huang, B., & Lin, H. (2021). Surface response and subsurface features during the restriction of groundwater exploitation in Suzhou (China) inferred from decadal SAR interferometry. *Remote Sensing of Environment*, 256, 112327.
- Tang, C. H., Hsu, Y. J., Barbot, S., Moore, J. D., & Chang, W. L. (2019). Lower-crustal rheology and thermal gradient in the Taiwan orogenic belt illuminated by the 1999 Chi-Chi earthquake. *Science advances*, 5(2), eaav3287.
- Tang, C. H., Barbot, S., Hsu, Y. J., & Wu, Y. M. (2020). Heterogeneous Power-Law Flow with Transient Creep in Southern California Following the 2010 El Mayor-Cucapah Earthquake. *Journal of Geophysical Research: Solid Earth*, 125(9), e2020JB019740.
- Wang, M., & Shen, Z. K. (2020). Present-day crustal deformation of continental China derived from GPS and its tectonic implications. *Journal of Geophysical Research: Solid Earth*, 125(2), e2019JB018774.
- Wen, Y., Li, Z., Xu, C., Ryder, I., & Bürgmann, R. (2012). Postseismic motion after the 2001 Mw 7.8 Kokoxili earthquake in Tibet observed by InSAR time series. *Journal of geophysical research: solid earth*, 117(B8).
- Weiss, J. R., Walters, R. J., Morishita, Y., et al. (2020). High-resolution surface velocities and strain for Anatolia from Sentinel-1 InSAR and GNSS data. *Geophysical Research Letters*, 47(17), e2020GL087376.

- Zhao, D., Qu, C., Bürgmann, R., Gong, W., & Shan, X. (2021). Relaxation of Tibetan Lower Crust and Afterslip Driven by the 2001 Mw7.8 Kokoxili, China, Earthquake Constrained by a Decade of Geodetic Measurements. *Journal of Geophysical Research: Solid Earth*, 126(4), e2020JB021314.
- Zhao, D., Qu, C., Bürgmann, R., Gong, W., Shan, X., Qiao, X., Chen, H., Liu, L. (2022) Large-scale Crustal Deformation, Slip-Rate Variation and Strain Distribution along the Kunlun Fault (Tibet) from Sentinel-1 InSAR Observations (2015-2020). *Journal of Geophysical Research: Solid Earth*, e2021JB022892.
- Zhu, L., Ji, L., & Liu, C. (2021). Interseismic slip rate and locking along the Maqin–Maqu Segment of the East Kunlun Fault, Northern Tibetan Plateau, based on Sentinel-1 images. *Journal of Asian Earth Sciences*, 211, 104703.